Nuclear Engineering and Technology 57 (2025) 103555

Contents lists available at ScienceDirect

Nuclear Engineering and Technology

journal homepage: www.elsevier.com/locate/net

Original Article

Manufacturing B_4C-Al dispersion absorber plates using the picture-frame technique

Sérgio Ricardo Catharino de Mello, Mauricio Moralles, Marco Antonio Stanojev Pereira, Frederico Antonio Genezini, Elita Fontenele Urano de Carvalho, Michelangelo Durazzo *

Nuclear and Energy Research Institute, IPEN-CNEN/SP, São Paulo, SP, Brazil

ARTICLE INFO

Keywords:
Neutron absorber materials
Boron carbide
Dispersions
Rolling
Neutron attenuation
Fabrication

ABSTRACT

The rising global demand for nuclear energy emphasizes the importance of neutron absorber materials, essential for spent fuel storage and other nuclear applications. This study focuses on manufacturing neutron absorber plates using the picture-frame technique, incorporating varying B_4C volume contents on an aluminum matrix in the plates' meat. Three configurations were explored, and the plates underwent radiographic, mechanical, microstructural, and neutronic evaluations. The results confirmed the viability of producing neutron absorber plates with reduced dimensions using the picture-frame method. Material properties were comparable to those of commercial neutron absorbers, indicating scalability for larger sizes, and facilitating the eventual deployment of this product. Plates with 45 vol% B_4C demonstrated favorable neutron shielding properties, achieving 100 % attenuation in a thermal neutron beam with a 4.0 mm thick B_4C-Al dispersion. However, adding B_4C to the aluminum matrix caused a decline in mechanical performance, with elongation values around 2 %, making these plates unsuitable for structural use, similar to other commercial materials in this category.

1. Introduction

With the continuous advancement of technology, electrical energy becomes increasingly important for the quality of human life. Several studies show how energy consumption is directly related to the economic growth of countries and regions [1–3]. A substantial portion of the world's current energy consumption is sourced from the combustion of fossil fuels. These resources are finite in nature and are notorious for their role in emitting greenhouse gases, which in turn contribute significantly to global warming. In this scenario, nuclear energy presents itself as a good alternative due to its favorable ratio between the amount of fuel used and the energy obtained, as well as not emitting these types of gases during the generation of electrical energy.

Nuclear energy generation consists of converting the heat generated by a nuclear reaction into electrical energy. The fissile material is placed in structures called fuel elements, which are distributed in the reactor core in sufficient quantities for the projected energy production. These structures and the reactor core design ensure that the fission reaction occurs in a controlled manner and allow for the safe shutdown of the reactor whenever necessary. Despite not emitting greenhouse gases during energy generation, waste management is a challenge for the widespread use of nuclear energy. After its use in the reactor, the used fuel generates heat and emits radiation spontaneously, requiring great care in its handling and storage.

Used fuel storage takes place through two fundamental methods: wet storage, where it is stored in pools, and dry storage. As soon as it is removed from the reactor, the used fuel is transferred to a large storage pool. Pool storage is a critical component for dissipating the heat generated by the radioactive decay of used fuel while also offering effective radiation shielding [4,5]. Dry storage is typically used after wet storage for fuels that have already undergone decay and reduced their activity. It involves placing the used fuel elements in a passively cooled casing that relies on natural conduction and convection to maintain the fuel elements at low temperatures [4,6]. Both wet and dry storage use neutron-absorbing materials to ensure that the materials do not reach criticality conditions [7].

For these reasons, the development of solutions and materials for the safe storage of irradiated fuel in nuclear reactors, whether in wet or dry storage conditions, becomes increasingly important. In general, these solutions consist of designing structures composed of neutron-absorbing

* Corresponding author. 2242, Cidade Universitária, CEP 05508-000, São Paulo, SP, Brazil.
E-mail addresses: srcmello@gmail.com (S.R. Catharino de Mello), moralles@ipen.br (M. Moralles), mstanojev1969@gmail.com (M.A.S. Pereira), fredzini@ipen.br (F.A. Genezini), elitaucf@ipen.br (E.F. Urano de Carvalho), mdurazzo@ipen.br (M. Durazzo).

https://doi.org/10.1016/j.net.2025.103555
Received 17 December 2024; Received in revised form 22 January 2025; Accepted 21 February 2025
Available online 22 February 2025

materials with dimensions suitable for each fuel project, which will serve as neutron shielding to allow the safe storage of fuel during its decay process after operation in a nuclear reactor. Neutron-absorbing materials consist of a chemical form of the neutron-absorbing nuclide and a matrix that serves to retain the neutron-absorbing nuclide in the desired location. To produce a neutron-absorbing material for commercial applications, the selected nuclide is integrated into a matrix that can be metallic or non-metallic, providing a homogeneous distribution of the nuclide throughout the final product. The nuclide is typically incorporated as an intermetallic phase (e.g., AlB_2), a stable carbide (e.g., B_4C), or an oxide (e.g., Gd_2O_3) [8].

Both metallic and non-metallic matrix neutron-absorbing materials have been produced and used for irradiated fuel storage applications. In metallic matrix neutron absorbers, aluminum has been the most commonly used matrix, although stainless steel is another option used, especially outside the United States. Non-metallic matrix absorbers primarily include phenolic resins and silicone-based rubbers [8].

Aluminum alloys are lightweight and have good corrosion resistance. These characteristics make them suitable matrices for accommodating boron in neutron absorption applications. However, the solubility of boron in aluminum is limited, so the development of composites with an aluminum matrix and boron carbide (B_4C) particles, rather than dissolved boron, allows for higher boron loadings and, consequently, better neutron absorption properties [8].

The aluminum alloys used for neutron-absorbing materials typically belong to the AA1000, AA5000, or AA6000 series, depending on the mechanical strength requirements. When the aluminum content in the material (or in the meat, for cladded materials) is greater than 50 vol%, the material is classified as a metal matrix composite (MMC). This category encompasses most aluminum-boron composite neutron absorbers. When aluminum constitutes less than 50 vol% of the material, it is classified as a ceramic matrix composite (CMC) or a cermet [8].

Aluminum-boron composites can be cladded with aluminum, usually with the aim of protecting the meat against corrosion or physical damage. Degrading factors that could compromise the adhesion between the meat and the cladding, such as blistering, can occur. However, optimizing the production process can reduce this risk [8].

Neutron-absorbing materials with aluminum matrices can be manufactured (usually in the form of thin plates) by numerous methods. In one method, a preform with nearly maximum theoretical density can be produced by casting, followed by hot rolling to the final thickness. In another method, a fully dense cylindrical billet of aluminum and boron carbide is produced using powder metallurgy technology. These materials, commonly known as metal matrix composites (MMC), are extruded and cut into a preform and then hot-rolled to the final thickness. One of the most widely used neutron absorbers is Boral, manufactured through a series of hot rolling passes applied to a cubic aluminum ingot containing a mixture of aluminum and boron carbide powders. Boral is a composite material in sheet form, featuring an aluminum cladding and a meat composed of uniformly distributed boron carbide and aluminum particles. The boron carbide concentration in the Boral ranges from 35 % to 65 % by weight [8].

The production of nuclear fuel plates employed in research reactors traditionally uses the globally recognized “picture frame technique” [9–11]. This process is presently employed at IPEN-CNEN/SP (Nuclear and Energy Research Institute) for manufacturing fuels intended for Materials Testing Reactors (MTR) [12,13].

The manufacturing process of the plate begins with the production of the meat, also called briquette, for which powder metallurgy techniques are adopted. Based on the calculated mass of the meat, the masses of the constituents, in powder form, are separately dosed in the proportion that meets the specified quantities of uranium. Then, the powders are homogenized to form a uniform distribution. The homogenized powder mixture is pressed at room temperature to obtain meats using a hydraulic press. The pressing pressure must be adjusted to achieve the desired thickness and porosity.

The briquette is assembled within a frame plate, covered by two cladding plates, as illustrated in Fig. 1. Subsequently, the assembly undergoes TIG welding and rolling processes [11–13].

The welded assembly is heated in a furnace to 440 °C, initiating the hot rolling process. This process involves passing the material through rolling cylinders using a predefined program of passes. Between each hot rolling pass, the assemblies are returned to the furnace to maintain the processing temperature. The hot rolling process creates a metallurgical bond between all the components of the original assembly (meat/frame/cladding), resulting in a solid piece of aluminum with the meat perfectly isolated at its center. Fig. 1 also provides an illustrative diagram of the appearance and components of the plate obtained after rolling [12].

The primary objective of this study is to assess the feasibility of implementing the picture-frame technique for the production of B_4C-Al absorber plates at IPEN-CNEN/SP. The results indicate the viability of this technique. Moreover, the fabrication procedures employed for producing fuel plates could be adapted with minor adjustments. Absorber plates containing 45 vol% of B_4C exhibited optimal performance for shielding applications. A 4.0 mm thick meat containing 45 vol % B_4C within the B_4C-Al dispersion proved sufficient to achieve 100 % neutron attenuation in a thermal neutron beam. However, it is important to note that the mechanical properties experienced progressive degradation with the introduction of B_4C into the aluminum matrix. With elongation results hovering around 2 %, none of the tested B_4C concentrations showed to be suitable for structural applications, consistent with similar commercial materials.

2. Material and methods

2.1. Raw materials

The powders employed in the preparation of B_4C-Al meats consisted of commercially available boron carbide powder conforming to ASTM C750 Type 3, boasting an average particle size of 100 μm, and aluminum powder, alloy AA1100, characterized by an average particle size of 12 μm. Aluminum alloy AA6061 sheets were utilized for crafting the frames and cladding plates.

The particle size distribution of both the B_4C and aluminum powders was determined using the laser diffraction method. Three separate samples of boron carbide were analyzed, yielding average particle diameters of 100.7 μm, 99.7 μm, and 100.4 μm, with a comprehensive

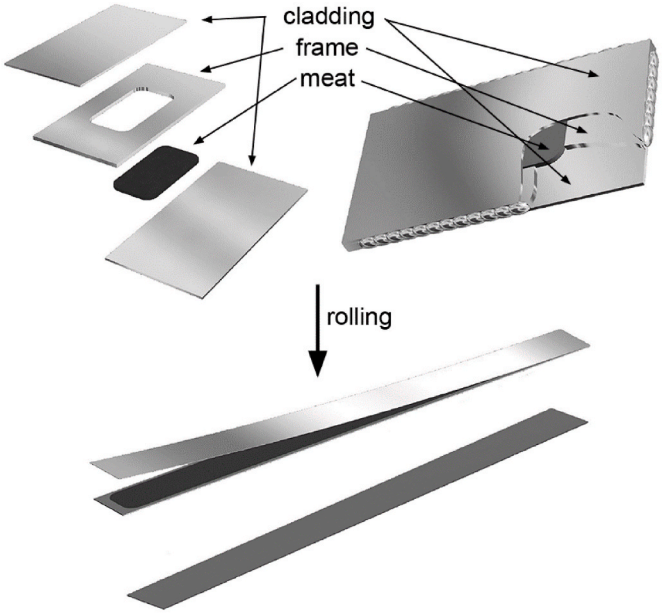

Fig. 1. Illustrative diagram depicting the picture-frame technique.

mean value of 100.3 μm. Fig. 2 illustrates a histogram depicting the average particle size distribution across these three samples of B_4C raw material.

To assess the particle size distribution of the aluminum powder more comprehensively, seven samples of this material were analyzed. The measurements yielded average diameters ranging from 11.49 μm to 12.30 μm, ultimately resulting in an aggregate mean value of 12.05 μm across all samples. The observed particles spanned sizes from 0.2 μm to 32 μm. Fig. 3 illustrates the histogram representing the average particle size distribution based on the seven samples of aluminum raw material employed.

The specific mass of the B_4C raw material was determined through helium pycnometry, yielding a result of 2.49 g/cm^3. This density, close to the theoretical value for boron carbide, suggests a low close porosity level in the raw material, estimated to be less than 1.2 vol%.

The scanning electron microscopy analysis performed on the raw material used for the meats allows for the observation of particle size distribution and morphology of these materials. The images showed intact grains without open porosities for the B_4C particulate. Figs. 4 and 5 show images, at different magnifications, depicting the morphology of the B_4C and aluminum powders used in this study.

2.2. Sample fabrication

In the production of B_4C-Al meats (briquettes), a floating square-sectioned die, measuring 2 × 2 cm, was employed for pressing the dispersion within a 25-ton hydraulic press.

The initial stage of the manufacturing process involved the blending of the B_4C and aluminum raw materials in precise proportions to attain the targeted volumetric fractions for each briquette. These volumetric fractions encompassed three levels, namely 15, 30, and 45 vol% of B_4C. The mass of each constituent in the mixture was calculated accounting for the densities of every component within the dispersion. Accurate quantities of each powder were measured using an analytical balance, and the blending of the raw materials was manually executed by agitating the materials inside an Erlenmeyer flask sealed with a lid.

Subsequently, the die was prepared for the pressing operation by applying zinc stearate to the punch surfaces and the sides of the floating body. Zinc stearate serves as a lubricant, mitigating excessive friction between the briquette and the die throughout the pressing and extraction processes.

After the preparation, the die was placed within a floating base, enabling vertical mobility of the die body while keeping the punch ends securely in place. This complete setup was then situated within the hydraulic press for vertical compression, as illustrated in Fig. 6. To initiate the pressing operation, a 25-ton load was uniformly applied to all briquettes through the activation of the hydraulic cylinder of the press, resulting in an approximate pressure of 5.5 t/cm^2 (550 MPa). This pressure was sustained for approximately 1 min to facilitate the accommodation and thorough pressing of the briquette.

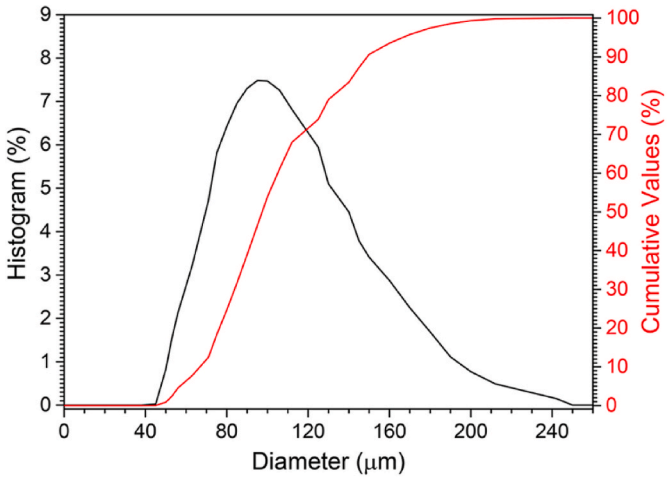

Fig. 2. Histogram depicting the particle size distribution of the B_4C raw material utilized.

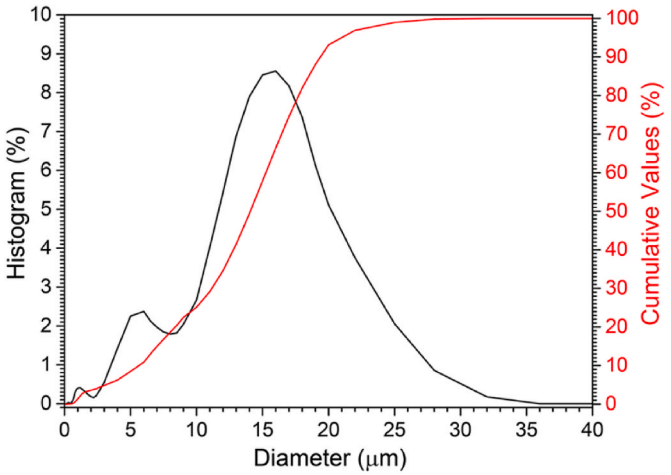

Fig. 3. Histogram depicting the particle size distribution of the aluminum powder utilized.

To extract the briquette from the die without compromising its structure, a two-piece extraction assembly was employed. This setup effectively transferred the hydraulic load solely to the die body, facilitating the seamless extraction of the briquette. Fig. 7 provides a glimpse of the B_4C-Al meat immediately after its extraction from the pressing die.

The production process for the absorber plates commences with the fabrication of the frame. Employing CNC (Computer Numeric Control) machining, a frame constructed from aluminum alloy AA6061 was machined to incorporate twelve cavities, each matching the dimensions of the meats produced. A clearance of 0.1 mm was maintained around these cavities to ensure the smooth and secure assembly of the B_4C-Al meats within the frame. Prior to assembling the meats, both the frame and cladding plates underwent a cleaning process to ensure residue-free surfaces, thus preventing any potential hindrance to bonding during the subsequent hot rolling phase. The presence of residues, dirt, or oxidation can impede contact between surfaces, leading to suboptimal adhesion between the cladding plates, meat, and frame. Following this, the assembly of the meats into the frame cavities was executed, as depicted in Fig. 8.

Altogether, twelve absorber plates were produced, each with meats comprising three distinct volumetric concentrations of B_4C. The concentrations under examination in this study were 15 vol%, 30 vol%, and 45 vol% of B_4C, and for each concentration, four replicate plates were crafted.

After the assembly of the meats and cladding plates, the welding process of the assembly was carried out. The frame and cladding plates were welded using the TIG (Tungsten Inert Gas) process without the addition of metal. Welding serves the purpose of maintaining the relative position between the parts during the initial rolling passes before the plates are fully bonded. The ends on all sides of the assembly were not welded to allow for the release of air during the rolling process, preventing defects such as blisters.

The welded assemblies were placed in the furnace and preheated for 1 h at 440 °C. The rolling process consisted of 8 hot rolling passes, with the first two passes having a 25 % reduction, and the subsequent passes with a 20 % reduction, reaching the final thickness of 1.55 mm. Between each rolling pass, the material was returned to the 440 °C furnace for 15 min. Simultaneously with the absorber plate manufacturing process, an equivalent-sized set of pure aluminum was also rolled to be used as a comparative reference during the characterization tests. Fig. 9 illustrates

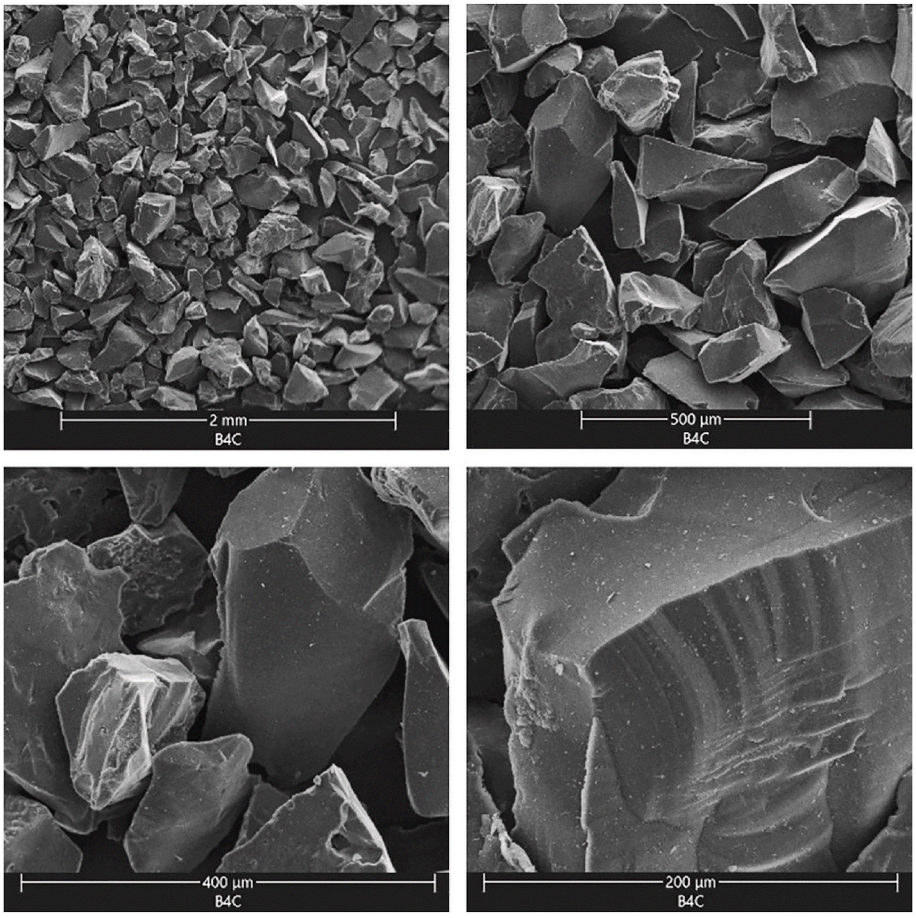

Fig. 4. Scanning electron micrographs (secondary electron images) illustrating the characteristic morphology of B_4C powder.

the hot rolling process of the plates.

2.3. Sample characterization

The initial characterization of the absorber plates involved visual inspection to check for the presence of blisters or any type of surface discontinuity that could be observed with the naked eye. Next, X-rays were used to inspect the meats to confirm the absence of cracks and check the continuity and uniformity of the meat.

Characterization of the mechanical properties was conducted through tensile testing using a universal testing machine from Instron. Due to the difficulty in machining the B_4C-containing meats, rectangular test specimens representing an entire section of the produced plate were manufactured. For comparative purposes, rectangular test specimens and standard test specimens according to ASTM E8/E8M were also manufactured containing no meats, with the same rolling history as the absorber plates and the same alloy.

The test specimens were subjected to standardized tensile tests, following ASTM E8/E8M, with a constant deformation rate of 0.04 mm/min. Yield strength and ultimate tensile strength data were automatically obtained by the testing machine's control system, while elongation was determined by measuring the difference in length of the gauge section of the specimen before and after the test.

Microstructural characterization was performed using scanning electron microscopy (SEM). These tests allowed for the observation of the level of homogeneity and the distribution of particles throughout the meat of the absorber plate, as well as the measurement of the meat and cladding thickness.

Samples for metallography were extracted for all three B_4C concentration conditions within the absorber plate meat. The samples were embedded and underwent a sequence of grinding using abrasives with grit sizes of 220, 320, 500, and 600, followed by polishing with diamond paste of 6 µm and 3 µm. A specialized program developed for measuring fuel plates, based on the Buehler OMNIMET software, was used for measuring the thickness of the meat and claddings. This program was capable of identifying the regions of the meat and claddings by image contrast and drawing 25 vertical lines on each image. The software measured the length of the line belonging to each identified region, allowing for individual measurement of the meat, upper cladding, and lower cladding thicknesses of the absorber plates. This procedure was repeated for four different regions, totaling 100 thickness measurements for each B_4C concentration condition. Fig. 10 displays representative microstructures of B_4C-Al dispersions across the three distinct volume fractions of B_4C. Fig. 11 delineates the procedure for measuring both the meat and cladding thickness of the absorber plate.

Neutron radiography (2D) and neutron tomography (3D) techniques were used for qualitative evaluation of neutron absorption along the test specimen, and a neutron counting technique was employed for quantitative assessment of the neutron beam attenuation capacity of the absorber plates. The characterization of the neutron properties of the absorber plates was carried out at the IEA-R1 nuclear research reactor located at IPEN.

The neutron tomography equipment located at Beam-Hole (BH) #14 of this reactor was utilized to obtain the neutron images. In Fig. 12, a depiction of the internal details of the irradiation position is presented. For comprehensive information on the equipment and tomography procedures, please refer to the detailed descriptions provided in the literature [14,15].

As the absorber material was placed as an obstacle to the neutron beam, the excitation of the scintillator was reduced in this region,

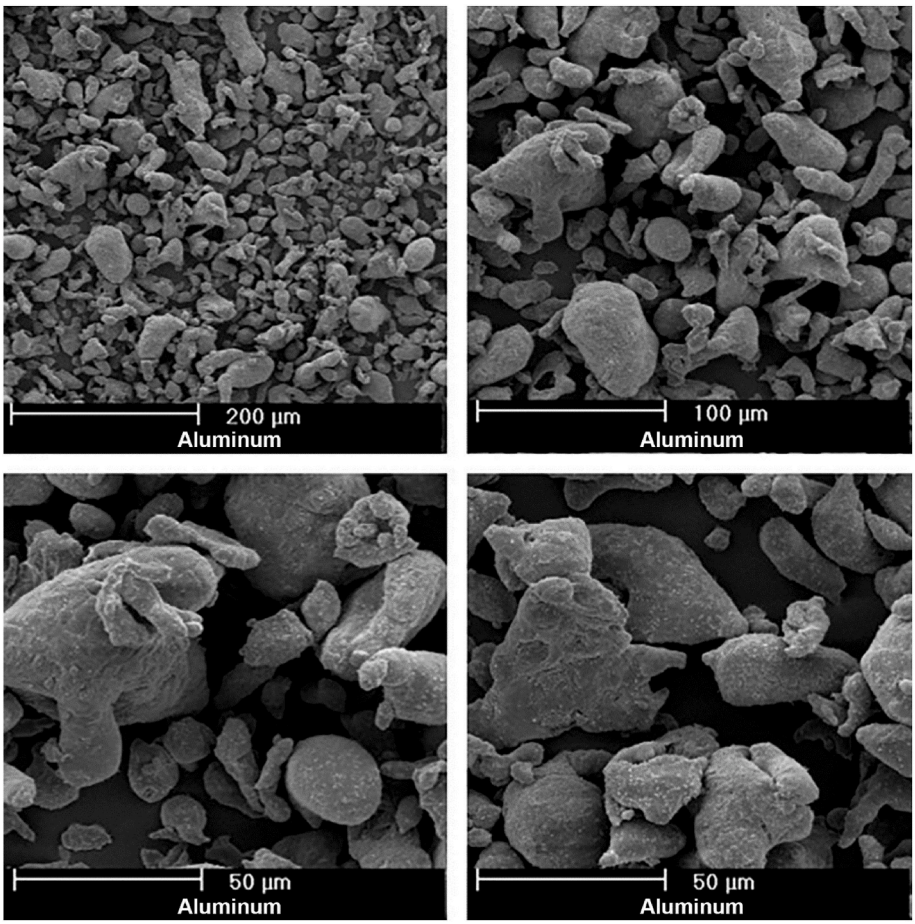

Fig. 5. Scanning electron micrographs (secondary electron images) illustrating the characteristic morphology of aluminum powder.

producing an image with different gray levels. The camera's software can measure the intensity of each of these gray levels, allowing for a more precise evaluation of the neutron absorption property of each region of the sample, enabling a comparison between different samples. In this way, it was possible to assess the uniformity of the distribution of the absorber element throughout the interior of the absorber plate. A pure aluminum test specimen was used as a reference to calibrate the equipment.

2.4. Neutron attenuation measurements

The effectiveness of a neutron-absorbing material is gauged by its neutron attenuation (*NA*), which represents the fraction of neutrons it can effectively block from traversing through it. Neutron attenuation is measured using a collimated and monoenergetic thermal neutron beam that impinges directly on the neutron-absorbing material. The intensities of the incident beam (I_i) and the beam transmitted through the material (I_t) are measured, and neutron attenuation (*NA*) can be calculated using Eq. (1). Neutron attenuation depends on the areal density of the neutron-absorbing nuclide and its morphology within the material [8].

$$NA = 1 - \frac{I_t}{I_i} \tag{1}$$

The relation between the intensities of the transmitted beam (I_t) and the incident beam (I_i) is commonly referred to as the transmission factor (T). This macroscopic property is employed by various researchers to characterize neutron-absorbing materials, particularly for graphical representation illustrating the variation in the transmission factor concerning the material's thickness [16–18]. Eq. (2) presents the mathematical expression for computing the transmission factor.

$$T = \frac{I_t}{I_i} \tag{2}$$

The macroscopic cross-section (Σ) plays a pivotal role in determining the neutron absorption characteristics of specimens. This parameter signifies the probability of any interaction occurring per unit thickness of the material through which the neutron is passing [16].

The intensity of the transmitted beam (I_t), the intensity of the incident beam (I_i), the thickness of the material (x), and the macroscopic cross-section (Σ) can be related through the Beer-Lambert law, as shown in Eq. (3) [16,19]. By substituting Eq. (2) into Eq. (3), it is possible to obtain the relationship between the transmission factor and the total macroscopic cross-section, as expressed in Eq. (4).

$$I_t = I_i e^{-\Sigma_t x} \tag{3}$$

$$T = e^{-\Sigma_t x} \tag{4}$$

A Texlium-type neutron detector in conjunction with a cadmium collimator and an electronic neutron counting system was used to quantitatively assess the neutron attenuation (*NA*) capacity of the absorber plates, we employed. The detector's surface was coated with cadmium sheets, leaving a single 5 mm diameter aperture aligned with the direction of the neutron beam. This design ensured that the detector's count primarily quantifies the presence of neutrons that successfully traversed the absorber plate samples, positioned as obstructions in the beam's trajectory.

At the beginning of the tests, a counting sequence was performed with no sample to be used as a reference for the maximum count value of the beam. A counting sequence with a 1.0 mm cadmium sample was

Fig. 6. Pressing system showing the floating die.

Fig. 7. Photograph depicting a representative B_4C-Al briquette.

used as the background reference (*BG*). This cadmium sample was made from the same material used for shielding the sensor and other equipment that should not be exposed to neutron incidence. The *BG* represents the background count for the test environment, i.e., the minimum count that the detector could register in the test configuration due to receiving neutrons from reflections or sources other than the collimator

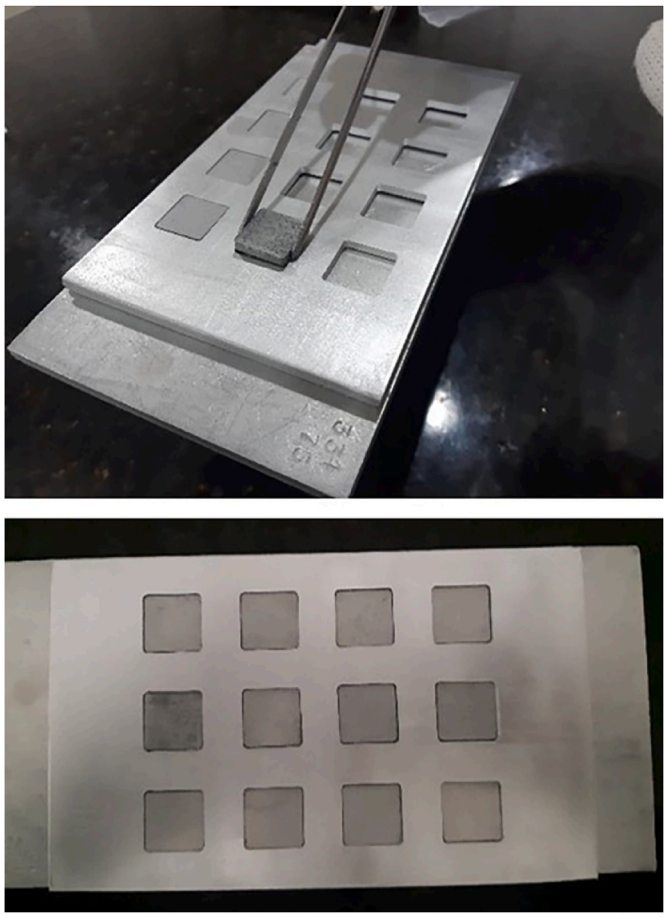

Fig. 8. Assembly of the meats into the frame cavities.

Fig. 9. Rolling process for the absorber plates.

used to generate the main beam.

This information is of fundamental importance to calculate the attenuation provided by each assembly of absorber plate samples. To calculate the attenuation value of the measured assembly, Eq. (1) was

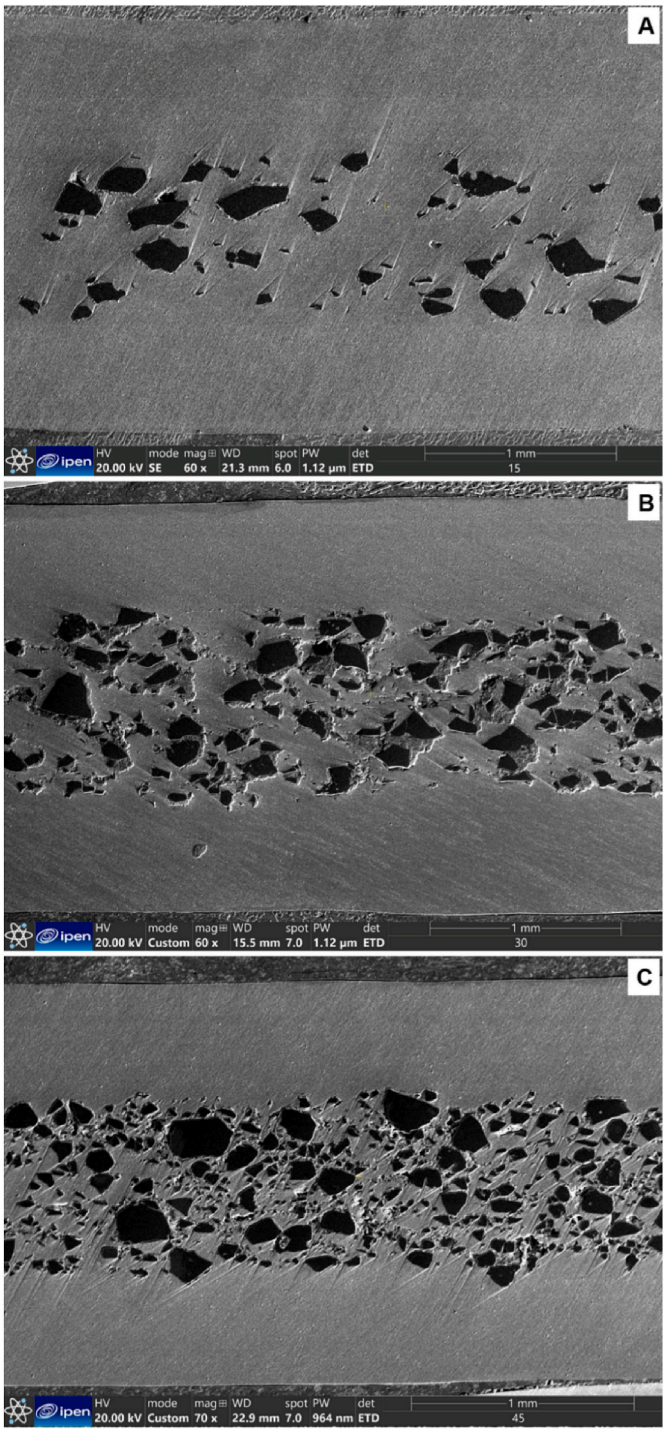

Fig. 10. Representative microstructures of B_4C-Al dispersions: A-15 vol% B_4C, B-30 vol% B_4C, C-45 vol% B_4C.

modified by substituting the transmitted intensity field (I_t) with the difference between the found count value (I) and the *BG* value. Similarly, the incident intensity field (I_i) was replaced by the difference between the maximum count value (I_{max}, corresponding to the assembly without a sample) and the *BG* value. In other words, the *BG* value was subtracted from both the incident and transmitted neutron beam counts. This correction resulted in Eq. (5).

$$NA = 1 - \left(\frac{I - BG}{I_{max} - BG}\right) \tag{5}$$

The neutron attenuation (*NA*) tests were conducted under four different conditions: pure aluminum plate, absorber plate with 15 vol% B_4C, absorber plate with 30 vol% B_4C, and absorber plate with 45 vol% B_4C. For each material condition, six thickness configurations were created. Six samples were taken from each of the absorber plates and the pure aluminum plate. The thickness configurations involved stacking samples of the same material to simulate behavior from 1 to 6 thicknesses. For each configuration, three neutron count measurements were taken over 30-s intervals. The average of these measurements was used to calculate the neutron attenuation of the configuration under analysis. Fig. 13 illustrates the assembly of the neutron attenuation test setup.

In addition to the overall attenuation results of the samples, which involve the contribution of the claddings and the meats of the absorber plates, the Beer-Lambert law was used to determine the total macroscopic cross-section (Σ_t) for both the claddings and the meats.

The first step was to use the irradiation results of pure aluminum to define the macroscopic cross-section of the material used as the cladding in the absorber plate. To calculate the value of the aluminum transmission factor, the field of transmitted intensity (I_t) in Eq. (2) was replaced by the difference between the measured count value (I) and the *BG* value. The field of incident intensity (I_i) was also replaced by the difference between the maximum count value (I_{max}, for the setup without samples) and the *BG* value, resulting in Eq. (6).

$$T = \left(\frac{I - BG}{I_{max} - BG}\right) \tag{6}$$

The transmission factor values obtained were associated with the thickness of the aluminum samples and represented graphically. A graphical feature of an exponential trend line was applied, which, once combined with the Beer-Lambert law represented by Eq. (4), allowed for the determination of the total macroscopic cross-section of the cladding material. Once this parameter was determined, it became possible to calculate the transmission factor for any thickness of the aluminum used. Therefore, the measured thickness values of the cladding were used to determine the transmission factor for the claddings of the absorber plates.

Once the transmission factor value for the aluminum cladding was determined, a process of separating the contributions from each region of the plate was carried out, as shown in Fig. 14. The absorber plate was considered as a sequence of three layers of material placed as an obstacle to the neutron beam.

During the experiments, values of incident beam and transmitted beam for the entire samples were recorded. The incident beam in the sample is equivalent to the incident beam in the first cladding, which represents the initial obstacle to the neutron beam. The beam transmitted through the first cladding is equivalent to the incident beam in the meat and was determined by multiplying the incident beam by the transmission factor of the first cladding. Using the same reasoning, the beam transmitted through the sample is equivalent to the beam transmitted through the second cladding, as it represents the final obstacle to the beam in that absorber plate. The value of the beam transmitted through the sample was divided by the transmission factor of the second cladding to determine the incident beam in the second cladding. Since the incident beam in the second cladding is equivalent to the beam transmitted through the meat, it was possible to obtain the values of incident and transmitted beam for each meat of the absorber plate, and consequently, it was possible to calculate the transmission factor for these meats.

As the experimental process consisted of sequential irradiations by adding samples of the same thickness to form different total thicknesses, an electronic spreadsheet with sequential calculation was used to determine the transmission factor of each B_4C-Al meat, segregating the contribution of its claddings to the attenuation of the neutron beam.

In this way, it was possible to determine the intensity of the incident beam (I_i) and the intensity of the transmitted beam (I_t) for each absorber

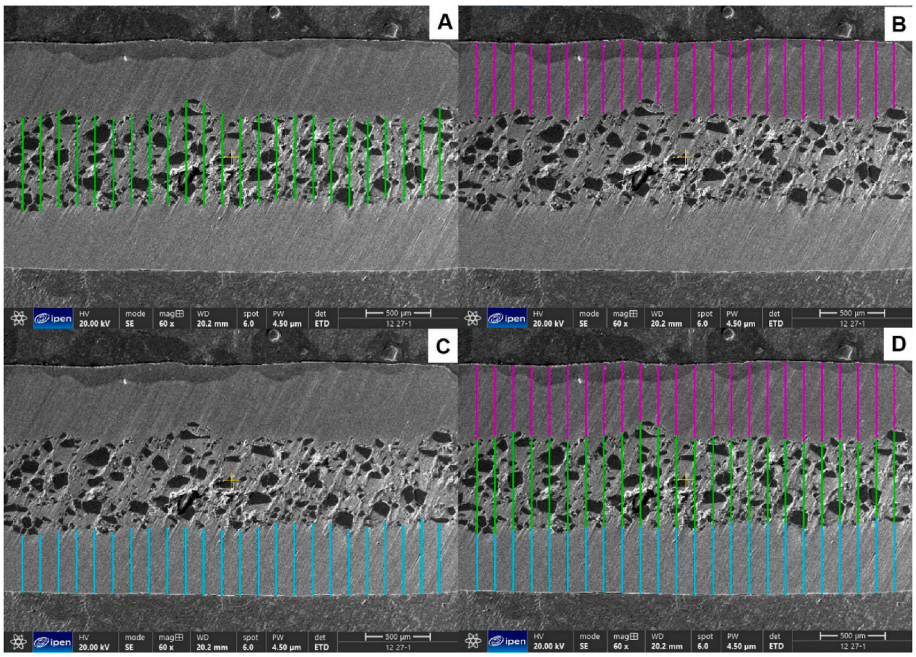

Fig. 11. Illustrative sequence for measuring thicknesses: A-meat, B-upper cladding, C-lower cladding, D-all layers.

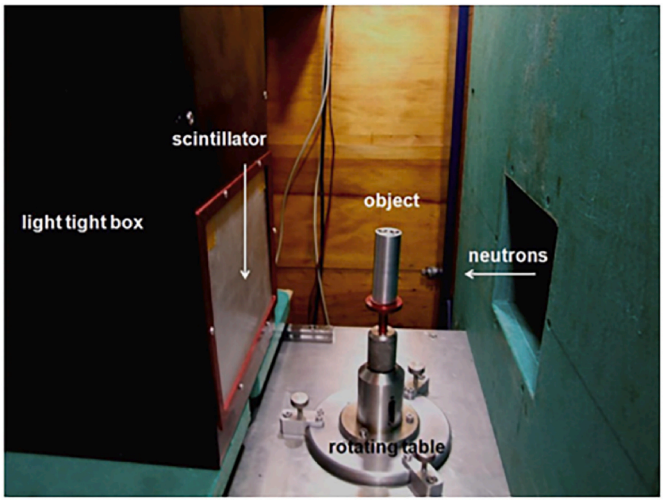

Fig. 12. Neutron tomography equipment utilized.

meat added to the experiment. For the calculation of the individual transmission factor (T) of each meat, the value of BG was corrected in Eq. (2), resulting in Eq. (7).

$$T = \left(\frac{I_t - BG}{I_i - BG}\right) \tag{7}$$

The calculation of the transmission factor was performed individually for each sample meat added to the experiment. Therefore, an average calculation was performed to determine the transmission factor for each concentration condition of B_4C in the meat.

The transmission factor results obtained were associated with the meat thickness results, measured by metallography. Eq. (4), which represents the Beer-Lambert law, was used to determine the total macroscopic cross-section for each meat condition produced in this study.

It was possible to estimate the behavior of the neutron properties such as the transmission factor and neutron attenuation for different thicknesses of absorber material meats by applying the values of total macroscopic cross-section in Eq. (4) and the values of the transmission factor in Eq. (1).

3. Results and discussion

The distribution of B_4C particles within the meats, across all three concentration conditions, is illustrated in Fig. 10. Despite the inherent fragility of B_4C particles, they display remarkable resistance to fragmentation and remain visibly intact throughout the rolling process. Typically, with fragile dispersed materials, a significant proportion of particles tend to fracture during rolling, resulting in a substantial increase in fine particles compared to the original powder. In such instances, the longitudinal section of the samples, aligned with the rolling direction (as in the case of the microstructures showed in Fig. 10), often exhibits the phenomenon known as “stringering.” This phenomenon involves the fragmentation of particles followed by the alignment of the resulting fragments. However, it is worth noting that this phenomenon is conspicuously absent in the case of B_4C.

The metallography of the material with a 15 vol% concentration of B_4C reveals a concern regarding the uniformity of neutron attenuation due to regions with a clear absence of absorber material, forming channels for free neutron transmission.

The SEM (Scanning Electron Microscopy) images were also used for measuring the thickness of each meat (see Fig. 11) to assess their behavior during hot rolling and for better sizing of neutron attenuation properties. Since there is no distinction between the claddings within the manufacturing process, the thickness data obtained from the micrographs were consolidated as claddings, and their means and standard deviations, as well as those of the meats of the absorber plates, are graphically presented in Fig. 15.

The first step in the study of the neutron properties of the absorber plates was the execution of neutron radiographs for each concentration condition of B_4C in the meat. A sample of pure aluminum was used to adjust the equipment so that the results obtained in the plate tests indicated exclusively the contribution of the B_4C-Al meats. The images in Fig. 16 show a gradual increase in the shade of gray as the concentration of B_4C in the meat of the absorber plate increases, as expected. However, the images also reveal problems with the uniformity of the distribution of absorber material along the length and width of the meat,

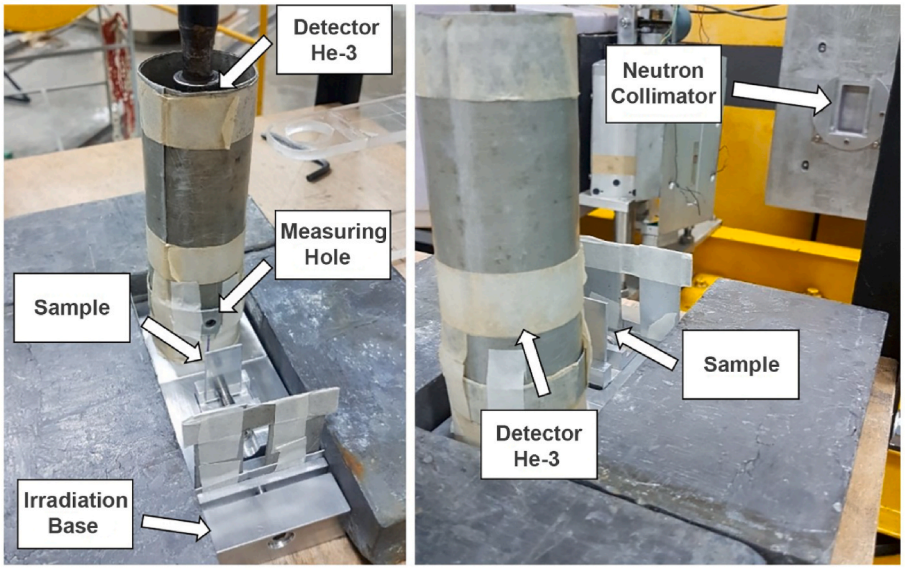

Fig. 13. Configuration of the neutron attenuation test setup.

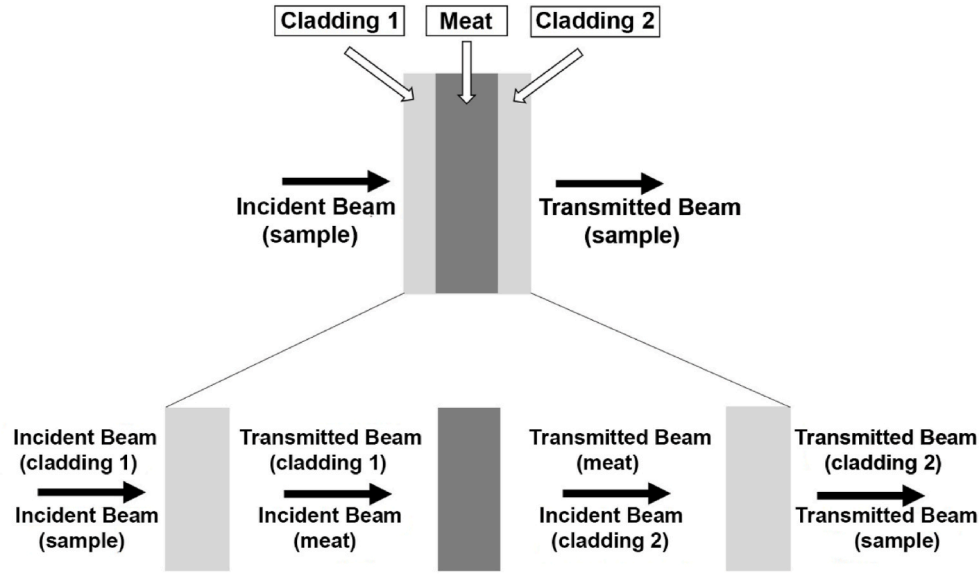

Fig. 14. Separation of contributions from claddings and meat for neutron attenuation.

due to the lighter spots scattered in the B_4C-Al meat region.

In addition to the neutron radiography analysis, with the use of the rotating base combined with image integration software, neutron tomography was also performed. This test generated three-dimensional images of the neutron absorption capacity of each meat, as shown in Fig. 17.

The findings from the tomographic scans further corroborated the previously identified issues concerning the homogeneous distribution of B_4C particles within the meats, as observed in both the neutrongraphy and metallography results. However, by virtue of its 3D viewer capability, tomography revealed that the challenges associated with achieving a homogeneous distribution of the absorber material are more pronounced in the cases of 15 vol% and 30 vol% B_4C concentrations within the meats. This observation suggests that the homogeneity issues within the meats are intricately linked to factors such as the quantity of absorber material, the distribution of B_4C particle sizes, and the methods employed in mixing the raw materials.

For the quantitative analysis of the neutron attenuation capacity of the absorber plates, a base of irradiation was used, exposed to a collimated beam of thermal neutrons, along with a He-3 type neutron detector for counting the transmitted beam. Combinations of up to 6 overlapping samples with the same concentration of B_4C were used, as well as measurements without samples and measurements with a cadmium plate. The results are summarized in Table 1, and the attenuation values were calculated according to Eq. (5), using the measurement without samples as I_{max} and the measurement with the cadmium plate as *BG*.

The absolute count values show coherence in the test, as samples representing the same boron-10 areal density have values of the same magnitude. For example, the assembly with 2 layers of 15 vol% B_4C had a similar count value (12342) to 1 layer of 30 vol% B_4C (12564). Similarly, 3 layers of 30 vol% B_4C have a count value (5921) of the same magnitude as 2 layers of 45 vol% B_4C (6152).

In addition to the neutron attenuation for the absorber plates, the individual contributions of the cladding were calculated. Table 2 presents the thickness values of pure aluminum samples, the average

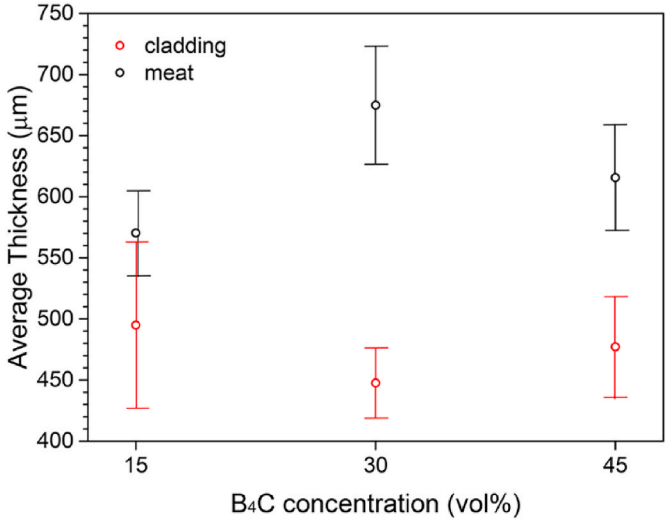

Fig. 15. Average cladding and meat thickness measured by metallography.

neutron counts, and the transmission factor of pure aluminum calculated using Eq. (6).

Fig. 18 presents the graphical correlation between the values of the transmission factor and the thickness of the aluminum sample in the test setup. An exponential trendline was fitted to the experimental data. By using the Beer-Lambert law, represented in Eq. (4), it was possible to determine the total macroscopic cross-section of the aluminum used, which has a value of 0.011 mm^{-1}.

Substituting the values of the cladding thickness found in the metallography and the total macroscopic cross-section value of aluminum in Eq. (4), the transmission factor for the cladding of each absorber plate produced was calculated, as shown in Table 3.

Once the transmission factor of the absorber plate claddings was determined, it was possible to create a sequential calculation spreadsheet capable of determining the transmission factor (T) individually for each meat of the absorber plate samples introduced in the neutron attenuation test. This calculation involved using the cladding transmission factor to determine the intensity of the incident beam (I_i) and the intensity of the transmitted beam (I_t) for each meat of the absorber plate sample added to the experiment and calculating its respective transmission factor value using Eq. (7).

Since the found transmission factor values were unique to each of the samples from the same absorber plate meat, an average transmission factor value ($T_{average}$) was calculated. The results obtained for the transmission factor of the absorber plate meats, along with the meat thickness observed in the metallography, were used to determine the total macroscopic cross-section (Σ_t) of each volumetric concentration condition of B_4C in the meats using the Beer-Lambert law, represented by Eq. (4). The results of this calculation are presented in Table 4.

Once the values of total macroscopic cross-section for each B_4C concentration condition were determined, it was possible to estimate the values of transmission factor and neutron attenuation for different meat thicknesses. The transmission factor values were calculated by applying the total macroscopic cross-section value to Eq. (4), and the neutron attenuation values were calculated by applying the transmission factor values to Eq. (1). Table 5 presents the estimated neutron properties values for meat thicknesses ranging from 0.25 to 10 mm. These values can be used in the design of applications for these materials in thermal

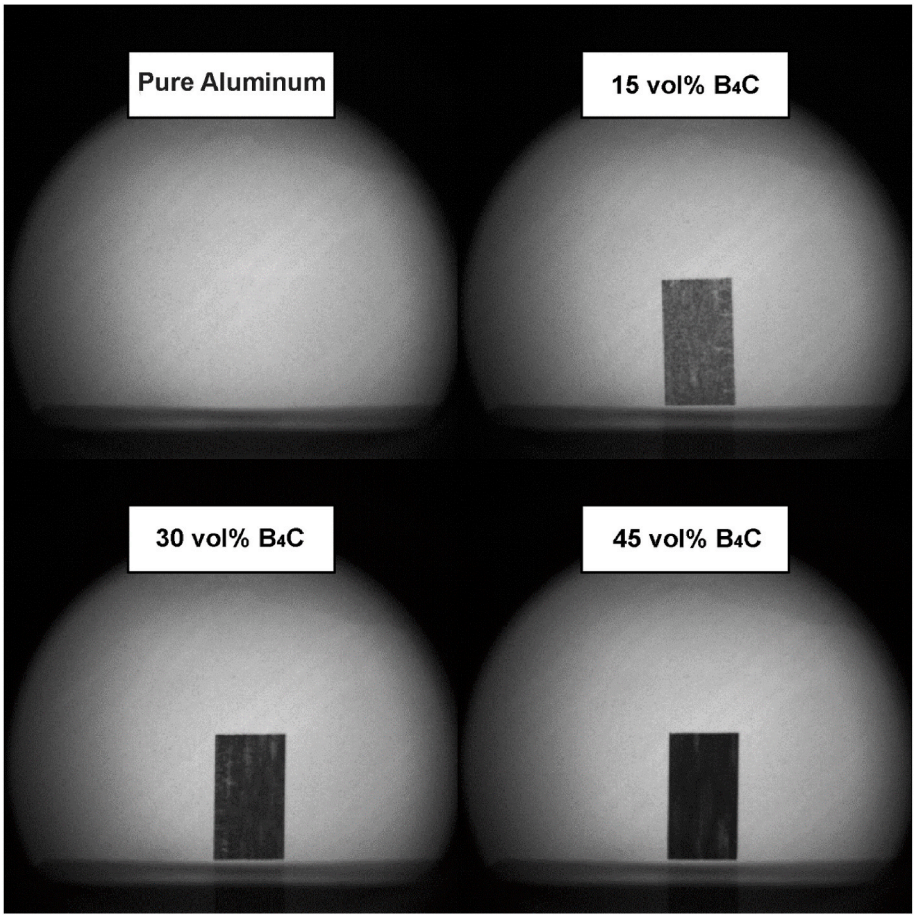

Fig. 16. Neutron radiography images of the absorber plates.

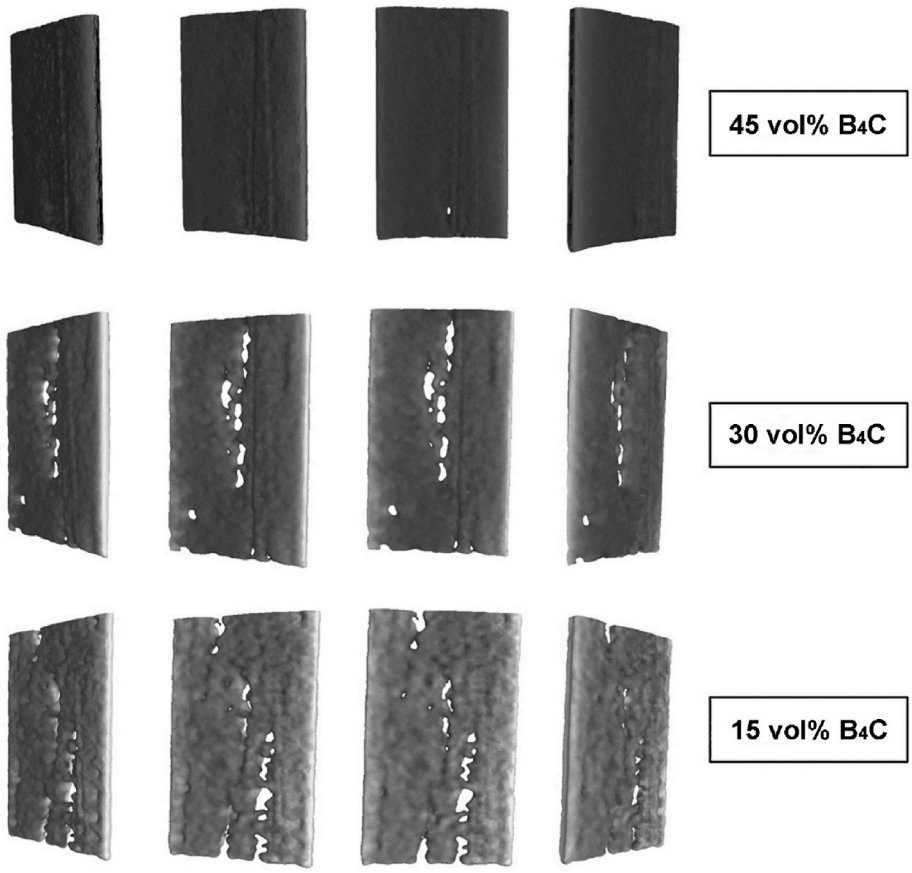

Fig. 17. Neutron tomography images of the B_4C-Al meats.

Table 1
Results of neutron transmitted count measurements through the samples (*NA*).

Sample	Sample Overlay	Measure 1 (counts)	Measure 2 (counts)	Measure 3 (counts)	Average (counts)	Standard Deviation (counts)	*NA* (%)	*NA* St. Dev. (%)
without sample	0	26108	26071	26132	26104	31	0.00	0.14 %
Pure Al	1	25119	25652	25529	25433	279	3.14	1.31
	2	24814	25105	24915	24945	148	5.43	0.69
	3	24672	24809	24669	24717	80	6.49	0.37
	4	24058	24418	25051	24509	503	7.47	2.35
	5	24030	24204	24465	24233	219	8.76	1.03
	6	23822	23730	24022	23858	149	10.51	0.70
15 vol% B_4C	1	17306	17479	17657	17481	176	40.37	0.82
	2	12412	12378	12236	12342	93	64.43	0.44
	3	9412	9356	9536	9435	92	78.04	0.43
	4	7607	7570	7471	7549	70	86.87	0.33
	5	6957	6841	6807	6868	79	90.05	0.37
	6	5777	5833	5612	5741	115	95.33	0.54
30 vol% B_4C	1	12560	12558	12574	12564	9	63.39	0.04
	2	8252	8220	8050	8174	109	83.94	0.51
	3	5895	5947	5920	5921	26	94.49	0.12
	4	5268	5098	5282	5216	102	97.79	0.48
	5	4950	4894	4823	4889	64	99.32	0.30
	6	4885	4909	4963	4919	40	99.18	0.19
45 vol% B_4C	1	9125	9337	9337	9266	122	78.83	0.57
	2	6032	6240	6184	6152	108	93.41	0.50
	3	4998	5196	5175	5123	109	98.23	0.51
	4	4852	4987	5017	4952	88	99.03	0.41
	5	4779	4858	4761	4799	52	99.74	0.24
	6	4726	4748	4807	4760	42	99.92	0.20
Pure Cd	1	4676	4659	4897	4744	133	100.00	0.62

neutron shielding conditions. The evolution of neutron attenuation values in relation to the thickness of the absorber plate meat is shown graphically in Fig. 19.

The estimated results of the neutronic properties show that it would require a 4 mm thickness of the material with 45 vol% B_4C to achieve 100 % neutron attenuation in a thermal neutron beam. Similarly, it would require a 6 mm thickness of the material with 30 vol% B_4C or a 10 mm thickness of the material with 15 vol% B_4C to achieve the same

Table 2
Aluminum transmission factor.

Thickness (mm)	Average Count	Transmission Factor
0	26104	1.00
1.55	25433	0.969
3.10	24945	0.946
4.65	24717	0.935
6.20	24509	0.925
7.75	24233	0.912
9.3	23858	0.895

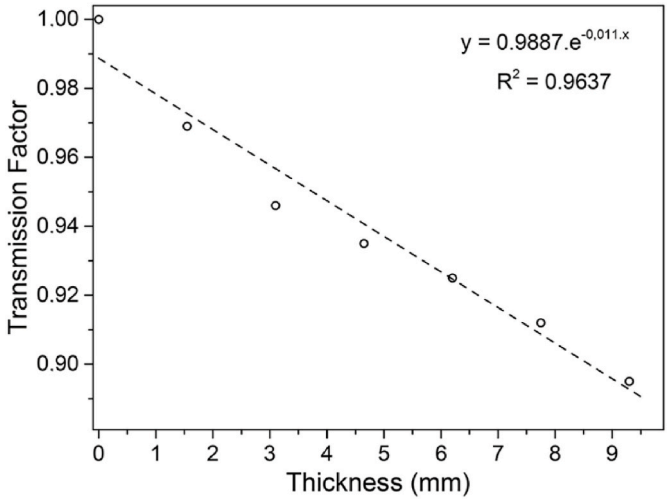

Fig. 18. Determination of the aluminum transmission factor.

Table 3
Cladding transmission factor of the absorber plates.

		Average Thickness (μm)	Transmission Factor
15 vol% B_4C	cladding 1	546.11	0.994
	cladding 2	443.58	0.995
30 vol% B_4C	cladding 1	443.00	0.995
	cladding 2	452.12	0.995
45 vol% B_4C	cladding 1	498.74	0.995
	cladding 2	455.67	0.995

Table 4
Total macroscopic cross-section (Σ_t) of the meats.

	Meat Average Thickness (μm)	Transmission Factor	Σ_t (mm^{-1})
15 vol% B_4C	570.31	0.621	0.835
30 vol% B_4C	674.88	0.397	1.367
45 vol% B_4C	615.59	0.277	2.084

condition.

The results of the tensile tests confirmed the non-structural characteristics of the material produced in this work, showing its similarity to other absorber materials used as references for the study. The results of yield strength, ultimate tensile strength, and elongation are summarized in Table 6.

Based on these results, it can be affirmed that the developed material cannot be used for structural purposes due to its low mechanical strength and, especially, the low elongation values. Projects involving this material should consider structural components to support the absorber plate.

Table 5
Estimated neutronic properties.

	Transmission Factor (%)			Neutron Attenuation (%)		
Thickness (mm)	15 vol% B_4C	30 vol% B_4C	45 vol% B_4C	15 vol% B_4C	30 vol% B_4C	45 vol% B_4C
0.25	0.812	0.711	0.594	18.8	28.9	40.6
0.50	0.659	0.505	0.353	34.1	49.5	64.7
0.75	0.535	0.359	0.209	46.5	64.1	79.1
1	0.434	0.255	0.124	56.6	74.5	87.6
2	0.188	0.065	0.015	81.2	93.5	98.5
3	0.082	0.017	0.002	91.8	98.3	99.8
4	0.035	0.004	0.000	96.5	99.6	100.0
5	0.015	0.001	0.000	98.5	99.9	100.0
6	0.007	0.000	0.000	99.3	100.0	100.0
7	0.003	0.000	0.000	99.7	100.0	100.0
8	0.001	0.000	0.000	99.9	100.0	100.0
9	0.001	0.000	0.000	99.9	100.0	100.0
10	0.000	0.000	0.000	100.0	100.0	100.0

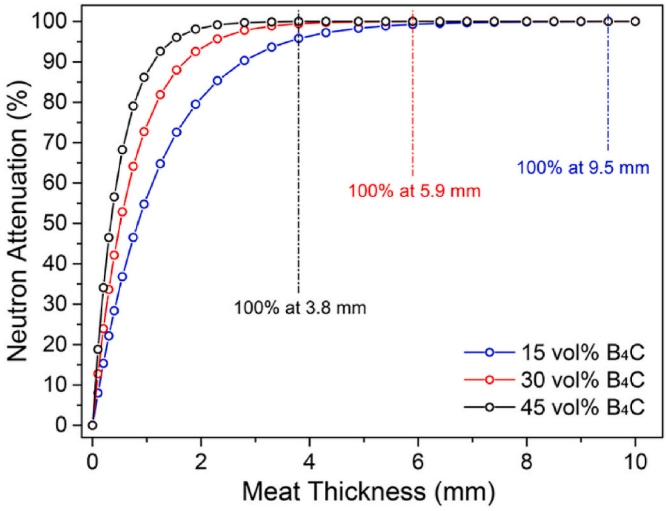

Fig. 19. Variation of neutronic attenuation with B_4C-Al meat thickness.

Table 6
Mechanical properties of B_4C-Al absorber plates.

Sample	vol% B_4C	Yield Strength (MPa)	Tensile Strength (MPa)	Elongation (%)
pure aluminum	0	99	123	8.8
	0	106	133	10.0
	0	101	130	9.0
	0	103	128	8.0
	0	110	136	6.6
	0	107	135	8.0
15 vol% B_4C	15	97	99	2.1
	15	96	97	0.8
	15	97	99	1.5
30 vol% B_4C	30	88	90	0.8
	30	90	91	0.8
	30	90	92	1.3
45 vol% B_4C	45	91	96	0.8
	45	89	89	0.6
	45	85	87	0.5

4. Conclusions

The results obtained in the development of this work indicate the feasibility of manufacturing absorber plates with B_4C-Al meats using the picture-frame technique, currently employed in the manufacturing of fuel plates. The pressing method used proved to be satisfactory for

producing intact B_4C-Al briquettes, suitable for the hot rolling process. The hot rolling process did not reveal any hindrances to producing the material in the dimensions used.

Metallography results revealed a microstructure similar to materials studied in the literature. The contrast between the particles was sufficient for the use of the developed software for fuel plates, allowing for precise measurement of meat and cladding thicknesses. The results also revealed challenges associated with particle distribution homogeneity in the absorber plate meats.

Neutrongraphy and neutron tomography results confirmed the challenges associated with particle distribution homogeneity in the meats, especially in the 15 vol% B_4C condition. However, the results of tests involving combinations of more than one sample showed a significant improvement in uniformity, suggesting that greater meat thicknesses exhibit greater neutron attenuation homogeneity.

Neutron attenuation results were promising, and the absorber plates exhibited suitable behavior for shielding applications. With simplified mathematical models, it was possible to estimate the properties of transmission factor and macroscopic cross-section for the different meat concentration conditions and project the required thicknesses for various shielding applications.

Mechanical properties were progressively degraded with the addition of B_4C to the aluminum matrix. Due to elongation results on the order of 2 %, none of the concentrations would allow for structural applications, as seen in similar commercial materials.

Overall, the results indicate a preference for using the condition with a 45 vol% B_4C concentration. Absorber plates with 45 vol% B_4C exhibited mechanical properties very similar to those of plates with 30 vol% B_4C concentrations and demonstrated superior neutron attenuation properties. The material with 15 vol% B_4C would have limited use due to requiring greater thicknesses and presenting an inferior meat homogeneity condition.

Ongoing future endeavors are focused on evaluating the feasibility of producing meats with larger dimensions, with the ultimate aim of enabling practical applications for this material. To enhance the homogeneity in particle distribution within the meats and, consequently, improve neutron-shielding performance, the utilization of B_4C raw materials featuring smaller particle sizes is recommended.

CRediT authorship contribution statement

Sérgio Ricardo Catharino de Mello: Validation, Methodology, Investigation, Data curation. **Mauricio Moralles:** Methodology, Investigation. **Marco Antonio Stanojev Pereira:** Validation, Methodology, Investigation. **Frederico Antonio Genezini:** Validation, Supervision, Conceptualization. **Elita Fontenele Urano de Carvalho:** Writing – original draft, Visualization, Validation. **Michelangelo Durazzo:** Writing – review & editing, Supervision, Project administration, Formal analysis, Conceptualization.

Data availability statement

The data that support the findings of this study are available from the corresponding author upon reasonable request.

Declaration of competing interest

The authors declare that they have no known competing financial interests or personal relationships that could have appeared to influence the work reported in this paper.

Acknowledgments

The authors are grateful to CNPq (National Council for Scientific and Technological Development) for the research grant 309826/2021–7 provided for this work. The authors would also like to thank São Paulo Research Foundation (FAPESP) for the research grant 2021/14331–5.

References

[1] D.I. Stern, Energy and economic growth in the USA: a multivariate approach, Energy Econ. 15 (2) (1993) 137–150, https://doi.org/10.1016/0140-9883(93)90033-N.
[2] W. Oh, K. Lee, Energy consumption and economic growth in Korea: testing the causality relation, J. Pol. Model. 26 (8–9) (2004) 973–981, https://doi.org/10.1016/j.jpolmod.2004.06.003.
[3] J. Chontanawat, L.C. Hunt, R. Pierse, Does energy consumption cause economic growth? Evidence from a systematic study of over 100 countries, J. Pol. Model. 30 (2) (2008) 209–220, https://doi.org/10.1016/j.jpolmod.2006.10.003.
[4] J.B. Wierschke, Evaluation of aluminum-boron carbide neutron absorbing materials for interim storage of used nuclear fuel. Doctor of Philosophy (Nuclear Engineering and Radiological Sciences), University of Michigan, 2015. https://hdl.handle.net/2027.42/111438.
[5] IAEA, Good practices for water quality management in research reactors and spent fuel storage facilities. IAEA Nuclear Energy Series, International Atomic Energy Agency, Vienna, 2011. No. NP-T-5.2, https://www-pub.iaea.org/MTCD/Publications/PDF/Pub1492_web.pdf.
[6] National Academy of Sciences, Safety and Security of Commercial Spent Nuclear Fuel Storage: Public Report, Washington D.C., 2006. https://nap.nationalacademies.org/catalog/11263/safety-and-security-of-commercial-spent-nuclear-fuel-storage-public.
[7] P. Zhang, Y. Li, W. Wang, G. Zhanping, B. Wang, The design, fabrication and properties of B_4C/Al neutron absorbers, J. Nucl. Mater. 437 (1–3) (2013) 350–358, https://doi.org/10.1016/j.jnucmat.2013.02.050.
[8] A. Machiels, R. Lambert, Handbook of Neutron Absorber Materials for Spent Nuclear Fuel Transportation and Storage Applications, Electric Power Research Institute, Palo Alto, CA, 2009. https://www.epri.com/research/products/000000000001019110.
[9] A.R. Kaufman, Nuclear Reactor Fuel Elements, Metallurgy and Fabrication, Interscience, New York, N.Y, 1962.
[10] Knight RW, Morin R.A. Fabrication procedures for manufacturing High Flux Isotope Reactor fuel elements II. Oak Ridge, Tenn., Oak Ridge National Lab., December 1999. ORNL-6852. https://doi.org/10.2172/757311.
[11] M. Durazzo, H.G. Riella, Procedures for Manufacturing Nuclear Research Reactor Fuel Elements, Lap Lambert Academic Publishing. OmniScriptum GmbH&Co, Saarbrücken, Germany, 2015.
[12] M. Durazzo, E. Vieira, E.F. Urano de Carvalho, H.G. Riella, Evolution of fuel plate parameters during deformation in rolling, J. Nucl. Mater. 490 (2017) 197–210, https://doi.org/10.1016/j.jnucmat.2017.04.018.
[13] M. Durazzo, J.A.B. Souza, E.F. Urano de Carvalho, T.A.G. Restivo, F.A. Genezini, R. M. Leal Neto, Manufacturing high-uranium-loaded dispersion fuel plates in Brazil, Ann. Nucl. Energy 200 (2024) 110408, https://doi.org/10.1016/j.anucene.2024.110408.
[14] M.A. Stanojev Pereira, R. Schoueri, C. Domienikan, F. Toledo, M.L.G. Andrade, R. Pugliesi, The neutron tomography facility of IPEN-CNEN/SP and its potential to investigate ceramic objects from the Brazilian cultural heritage, Appl. Radiat. Isot. 75 (2013) 6–10, https://doi.org/10.1016/j.apradiso.2013.01.030.
[15] Schoueri R, Domienikan C, Toledo F, Andrade MLG, Stanojev Pereira MA, Pugliesi R. The new facility for neutron tomography of IPEN-CNEN/SP and its potential to investigate hydrogenous substances. Appl. Radiat. Isot. 84, 201422-201426. https://doi.org/10.1016/j.apradiso.2013.10.019.
[16] S. Orak, D.Y. Baysoy, Neutron shielding properties of concrete with boron and boron containing mineral, Academic Plat. J. Eng. Smart Sys. APJES I-I (2013) 15–19. https://dergipark.org.tr/tr/download/article-file/25224.
[17] A.R. Rennie, A. Engberg, O. Eriksson, R.M. Dalgliesh, Understanding neutron absorption and scattering in a polymer composite material, Nucl. Instrum. Methods Phys. Res. 984 (2020) 164613, https://doi.org/10.1016/j.nima.2020.164613.
[18] A.S. Kipcak, D.Y. Baysoy, E.M. Derun, S. Piskin, Characterization and neutron shielding behavior of dehydrated magnesium borate minerals synthesized via solid-state method, Adv. Mater. Sci. Eng. (2013) 747383, https://doi.org/10.1155/2013/747383.
[19] D.R. McAlister, Neutron shielding materials. PG research foundation, inc. 1955 university lane lisle, IL 60532, USA. Revision 2.1. https://www.eichrom.com/wp-content/uploads/2018/02/neutron-attenuation-white-paper-by-d-m-rev-2-1.pdf, February 25, 2016.